

Fundamentals of Measurement in Terahertz Time-Domain Spectroscopy

Withawat Withayachumnankul · Mira Naftaly

Received: 1 October 2013 / Accepted: 26 November 2013 /
Published online: 12 December 2013
© Springer Science+Business Media New York 2013

Abstract Terahertz time-domain spectroscopy (THz-TDS) has emerged as a main spectroscopic modality to fill the frequency range between a few hundred gigahertz to a few terahertz. This spectrum has been known as “terahertz gap” owing to limited accessibility by conventional electronic and optical techniques. Over the past two decades, THz-TDS has evolved substantially with enhanced compactness and stability. Since THz-TDS is becoming an industrial standard, the performance and precision of the system are of prime importance. This article provides an overview on terahertz metrology, including parameter estimation, signal processing, measurement characteristics, uncertainties, and calibrations. The overview serves as guidance for metrology and further developments of THz-TDS systems.

Keywords THz-TDS · Terahertz metrology · Measurement characteristics · Uncertainties · Calibrations · Parameter estimation · Dynamic range

1 Introduction

Since the previous century, researchers have had a strong desire to bridge the terahertz gap, loosely defined between 0.1 and 10.0 THz. Very early attempts were based on black-body radiation from thermal sources. Over many decades afterwards, a variety of techniques had been developed, both from the microwave and optics communities.

W. Withayachumnankul (✉)
School of Electrical and Electronic Engineering, The University of Adelaide,
Adelaide, SA 5005, Australia
e-mail: withawat@eleceng.adelaide.edu.au

M. Naftaly
National Physical Laboratory, Hampton Road, Teddington, TW11 0LW, UK
e-mail: mira.naftaly@npl.co.uk

Despite that, most of the techniques shared common issues in the system efficiency, size, and stability. A new era of terahertz development followed the emergence of ultrafast lasers and semiconductors technologies. The synergy between these two advances led to the first terahertz photoconductive antenna by Auston et al. [1]. Years after, subsequent developments have led to an efficient approach to coherent terahertz generation and detection, now widely known as terahertz time-domain spectroscopy (THz-TDS). Its broadband measurement capability and strong immunity to background noise facilitate observation of terahertz-material interactions, which are attractive to researchers in a wide range of fundamental disciplines.

THz-TDS is unique in its way of measurement. Other spectroscopic modalities, such as vector network analyzers or IR-Vis-UV spectrometers, conduct measurement directly in the frequency domain via, e.g., frequency sweeping or broadband exposure. Fourier-transform infrared spectrometers (FTIRs) perform measurement indirectly in the time domain via interferometry. In contrast, THz-TDS is based on the direct time-domain sampling with an ultrafast-laser pump/probe configuration. This difference makes terahertz metrology distinctive and worth thorough consideration. Measurement characteristics, including the dynamic range, bandwidth, signal-to-noise ratio, and frequency resolution, are tied up with pulse behaviors. As the data are collected in the time domain, a special signal processing technique is required to extract meaningful frequency-dependent properties from measurements. Uncertainty evaluation is necessary to quantify impacts of error contributed by various sources along the measurement process. Generally, it is beneficial to be aware of these modality-specific aspects to gain more insight into data and to avoid false interpretation of results. Considering the prevalence of terahertz spectrometers in academia and industry, it is timely for this overview to put together these critical aspects of terahertz metrology.

This article overviews different aspects of terahertz metrology that have been extensively studied over the past decade. The overview serves as a basis for spectroscopists working with THz-TDS. It is assumed that the reader has some background in the operation of THz-TDS. In this article, Section 2 provides information on ray optics for transmission- and reflection-mode THz-TDS, from which a standard parameter estimation process is derived. A few essential signal processing techniques are discussed in detail. Section 3 discusses measurement characteristics specific to THz-TDS, along with their implications on the performance and accuracy. Sources of measurement error are discussed in Section 4 with an uncertainty analysis that forms a basis for measurement comparison and optimization. Calibrations of the systems is given in Section 5. Although the overview mainly focuses on transmission-mode THz-TDS, the concepts are general and applicable to other THz-TDS variants.

2 Material Characterization with Transmission-Mode THz-TDS

This section provides background on parameter estimation of dielectric materials with transmission-mode THz-TDS. The analytical model for wave propagation specific to this configuration will be shown to relate amplitude and phase changes in a

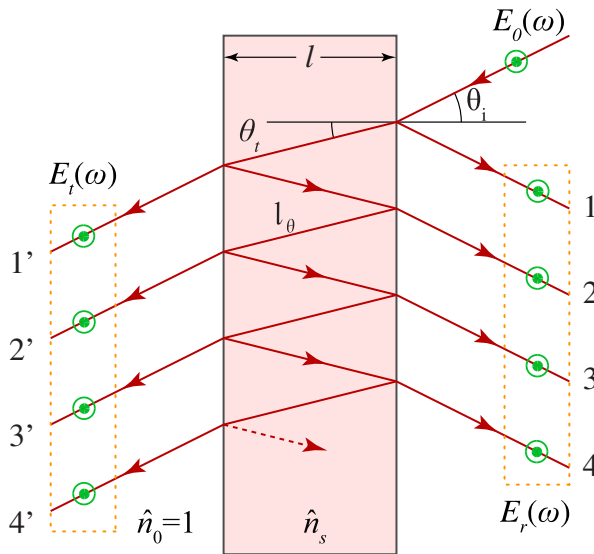


Fig. 1 Wave propagation model in a homogeneous dielectric slab. The refractive indices of the surrounding free space and dielectric are denoted by $\hat{n}_0 = 1$ and \hat{n}_s , respectively. In addition, $E_0(\omega)$ is the incident wave; θ_i is the incident angle; and θ_t is the refraction angle. The propagation distance l_θ is derived from the sample thickness l , and equals $l/\cos\theta_t$. The arrows show intermediate propagation paths grouped into the transmission, $1', 2', 3', \dots$, and the reflection, $1, 2, 3, \dots$

measured signal to the optical properties of materials. Based on this model, a standard parameter extraction method will be described in detail. Some signal processing methods commonly applied during the parameter extraction process are also given.

2.1 Wave Propagation Through Dielectric Slab

Figure 1 illustrates wave propagation through a homogeneous dielectric slab with a complex refractive index of \hat{n}_s and thickness of l . The refraction and reflection at the

Table 1 Multiplication factors for a propagating wave

Reflection path	Multiplication factor	Transmission path	Multiplication factor
1	ρ	1'	$\tau\tau'\exp\left[-j\hat{n}_s\frac{\omega l}{c}\right]$
2	$\tau\tau'\rho'\exp\left[-2j\hat{n}_s\frac{\omega l}{c}\right]$	2'	$\tau\tau'\rho'^2\exp\left[-3j\hat{n}_s\frac{\omega l}{c}\right]$
3	$\tau\tau'\rho'^3\exp\left[-4j\hat{n}_s\frac{\omega l}{c}\right]$	3'	$\tau\tau'\rho'^4\exp\left[-5j\hat{n}_s\frac{\omega l}{c}\right]$
4	$\tau\tau'\rho'^5\exp\left[-6j\hat{n}_s\frac{\omega l}{c}\right]$	4'	$\tau\tau'\rho'^6\exp\left[-7j\hat{n}_s\frac{\omega l}{c}\right]$
5	\dots	5'	\dots

The path numbers and other variables are associated with Fig. 1, and the normal incident angle is assumed. Here, $\tau = 2/(1 + \hat{n}_s)$ and $\rho = (1 - \hat{n}_s)/(1 + \hat{n}_s)$ are the complex transmission and reflection coefficients for the wave incident from free space. Likewise, $\tau' = 2\hat{n}_s/(1 + \hat{n}_s)$ and $\rho' = (\hat{n}_s - 1)/(\hat{n}_s + 1)$ are the transmission and reflection coefficients for the wave incident in the sample. After [2]

interfaces between the sample and free space result in multiple propagation paths in the dielectric slab. The wave taking each path in Fig. 1 has its expression determined by multiplication between the incident wave $E_0(\omega)$ and a corresponding factor. At each interface, the wave is modified by a Fresnel transmission or reflection coefficient. Inside the sample, the exponential term, representing the complex response of a material, has an influence on the propagating wave. Multiplication factors for all paths are given in Table 1.

In the case of normal incidence, where $\theta_i = 0$, all the transmission (reflection) paths overlap and $l_\theta = l$. The total transmitted wave is therefore summation of waves among the intermediate transmission paths. Following Table 1, the transmitted wave reads

$$\begin{aligned} E_t(\omega) &= \tau \tau' \cdot \exp \left[-j \hat{n}_s(\omega) \frac{\omega l}{c} \right] \\ &\quad \cdot \left\{ 1 + \rho'^2 \exp \left[-2j \hat{n}_s(\omega) \frac{\omega l}{c} \right] + \rho'^4 \exp \left[-4j \hat{n}_s(\omega) \frac{\omega l}{c} \right] + \dots \right\} \cdot E_0(\omega) \\ &= \tau \tau' \cdot \exp \left[-j \hat{n}_s(\omega) \frac{\omega l}{c} \right] \cdot \text{FP}(\omega) \cdot E_0(\omega), \end{aligned} \quad (1)$$

where $\text{FP}(\omega)$ represents the Fabry-Pérot effect as a consequence of reflections inside the sample, and is given as

$$\begin{aligned} \text{FP}(\omega) &= \left\{ 1 + \rho'^2 \cdot \exp \left[-2j \hat{n}_s(\omega) \frac{\omega l}{c} \right] + \rho'^4 \exp \left[-4j \hat{n}_s(\omega) \frac{\omega l}{c} \right] + \dots \right\} \\ &= \sum_{m=0}^{\infty} \left\{ \rho'^2 \cdot \exp \left[-2j \hat{n}_s(\omega) \frac{\omega l}{c} \right] \right\}^m \\ &= \left\{ 1 - \rho'^2 \cdot \exp \left[-2j \hat{n}_s(\omega) \frac{\omega l}{c} \right] \right\}^{-1}. \end{aligned} \quad (2)$$

In analogy to the total transmitted wave, the total reflected wave can be expressed as

$$\begin{aligned} E_r(\omega) &= \rho E_0(\omega) + \tau \tau' \rho' \cdot \exp \left[-2j \hat{n}_s(\omega) \frac{\omega l}{c} \right] \\ &\quad \cdot \left\{ 1 + \rho'^2 \cdot \exp \left[-2j \hat{n}_s(\omega) \frac{\omega l}{c} \right] + \rho'^4 \exp \left[-4j \hat{n}_s(\omega) \frac{\omega l}{c} \right] + \dots \right\} \cdot E_0(\omega) \\ &= \rho E_0(\omega) + \tau \tau' \rho' \cdot \exp \left[-2j \hat{n}_s(\omega) \frac{\omega l}{c} \right] \cdot \text{FP}(\omega) \cdot E_0(\omega). \end{aligned} \quad (3)$$

These basic equations relate a measurable spectrum with the material optical properties. These relations are essential in the parameter extraction and other analyses. Since THz-TDS carries out measurements in the time domain, obtainable terahertz signals must be converted to the frequency domain via Fourier transform before further processing. The reflections after the main pulse can be dealt with by using temporal windowing in the time domain or by taking into account the Fabry-Pérot term during parameter estimation.

2.2 Parameter Retrieval

Measurement of free-standing samples with THz-TDS was introduced by Grischkowsky et al. when they sought dielectrics that are suitable for making terahertz lenses [3]. Samples made of dielectrics preformed into slabs were measured in the transmission mode, and their optical constants were determined using curve fitting to the data. Later on, many iterative methods were proposed for extracting the parameters from the measurement. The method introduced by Duvillaret et al. models an error from the difference between the estimated and measured data at each frequency as a function of the optical constants [4]. The error curve is then approximated by a paraboloid, the global minimum of which determines a correct solution. That solution can be obtained by an iterative numerical procedure. A few more methods were suggested to estimate the optical constants together with the sample thickness [5–9]. The process simultaneously determines a set of the optical constants at various guessed thicknesses, and uses the criterion of the total variation of the optical constants to select the correct thickness. In this section, an approximated solution to the parameter extraction problem is elaborated.

Following Eq. 1, a terahertz signal that passes through a dielectric sample with parallel surfaces at a normal angle of incidence, assuming no reflections, can be expressed in the frequency domain as

$$E_{\text{sam}}(\omega) = \eta \frac{4\hat{n}_s(\omega)}{[\hat{n}_s(\omega) + 1]^2} \cdot \exp\left[-j\hat{n}_s(\omega)\frac{\omega l}{c}\right] \cdot E_0(\omega), \quad (4)$$

where η is the transmission factor of free space surrounding the sample. The complex refractive index of the sample $\hat{n}_s(\omega) = n_s(\omega) - j\kappa_s(\omega)$, where $n_s(\omega)$ is the refractive index and $\kappa_s(\omega)$ is the extinction coefficient. In addition to the sample spectrum,

$$E_{\text{ref}}(\omega) = \eta \cdot \exp\left[-j\frac{\omega l}{c}\right] \cdot E_0(\omega), \quad (5)$$

is the complex frequency spectrum of a reference signal, i.e., a signal measured with the same settings but in the absence of the sample.

The material parameter extraction process requires these two spectra, $E_{\text{sam}}(\omega)$ and $E_{\text{ref}}(\omega)$, which are Fourier transformed from time-domain measurements. Normalising the sample spectrum by the reference, or $E_{\text{sam}}(\omega)/E_{\text{ref}}(\omega)$, yields the complex transfer function of the sample in the frequency domain:

$$H_0(\omega) = \frac{4\hat{n}_s(\omega)}{[\hat{n}_s(\omega) + 1]^2} \cdot \exp\left\{-\kappa_s(\omega)\frac{\omega l}{c}\right\} \cdot \exp\left\{-j[n_s(\omega) - 1]\frac{\omega l}{c}\right\}. \quad (6)$$

Often the complex refractive index, $\hat{n}_s(\omega)$ that is a part of the Fresnel coefficients is approximated with a real index, $n_s(\omega)$, giving

$$H(\omega) = \frac{4n_s(\omega)}{[n_s(\omega) + 1]^2} \cdot \exp\left\{-\kappa_s(\omega)\frac{\omega l}{c}\right\} \cdot \exp\left\{-j[n_s(\omega) - 1]\frac{\omega l}{c}\right\}. \quad (7)$$

Taking the argument and logarithm of the simplified transfer function gives, respectively,

$$\angle H(\omega) = -[n_s(\omega) - 1] \frac{\omega l}{c}, \quad (8a)$$

$$\ln |H(\omega)| = \ln \left[\frac{4n_s(\omega)}{(n_s(\omega) + 1)^2} \right] - \kappa_s(\omega) \frac{\omega l}{c}. \quad (8b)$$

The optical constants of the sample can be deduced from Eq. 8a, b as

$$n_s(\omega) = 1 - \frac{c}{\omega l} \angle H(\omega), \quad (9a)$$

$$\kappa_s(\omega) = \frac{c}{\omega l} \left\{ \ln \left[\frac{4n_s(\omega)}{(n_s(\omega) + 1)^2} \right] - \ln |H(\omega)| \right\}. \quad (9b)$$

Further, the absorption coefficient $\alpha_s(\omega)$ is related to the extinction coefficient via

$$\alpha_s(\omega) = 2 \frac{\omega \kappa_s(\omega)}{c}. \quad (10)$$

Note that $H(\omega)$ is determined from the measurements of the sample and reference, and calculating $\angle H(\omega)$ requires a special phase unwrapping process, which will be discussed in Section 2.3.

2.3 Signal Processing Techniques

In this section, signal processing techniques typically applied to THz-TDS data are briefly discussed. These techniques include signal averaging and phase unwrapping. Zero-padding for truncated time-domain signals will be discussed in Section 3.3

2.3.1 Signal Averaging in the Time and Frequency Domains

Random noise in measurement can be reduced by averaging a series of signals obtained from multiple repeated measurements. The averaging is effective in the time domain, but not in the frequency domain [10]. This contrast is depicted in Fig. 2, where the noise floor reduces only in the case of time-domain averaging. As a result, the system dynamic range, to be discussed in Section 3.1, can be improved.

A mathematical explanation of the difference between averaging in the time and frequency domains is as follows. Given that $x_0(t)$ is a noise-free signal from a time-invariant system, and $n(t)$ is a random noise, which has a normal distribution around zero, the signal from the k^{th} measurement is expressed as

$$x_k(t) = x_0(t) + n_k(t). \quad (11)$$

An expectation $\langle x \rangle$ is defined for the variable x_k . Since $\langle n_k(t) \rangle = 0$,

$$\langle x_k(t) \rangle = x_0(t). \quad (12)$$

The expectation of a measured signal is noiseless. This implies that averaging the signals in the time domain decreases the noise.

Transforming the signal from Eq. 11 into the frequency domain yields

$$X_k(\omega) = X_0(\omega) + N_k(\omega), \quad (13)$$

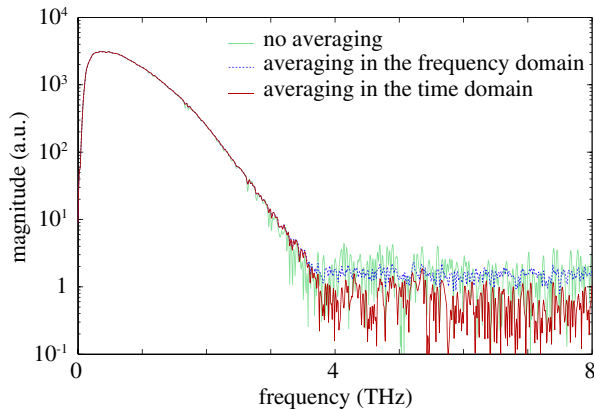


Fig. 2 Spectra averaged by using different schemes. Time-domain averaging is carried out with ten measurements. Averaging in the frequency domain is performed with the magnitude of the spectra. A proper averaging technique can significantly lower the noise floor, and thus increase the dynamic range and bandwidth

where $X_k(\omega)$, $X_0(\omega)$, and $N_k(\omega)$ are the Fourier pairs of $x_k(t)$, $x_0(t)$, and $n_k(t)$, respectively. Analogous to the expectation of a signal in the time domain, the expectation of a spectrum in the frequency domain results in a noise-free spectrum, or

$$\langle X_k(\omega) \rangle = X_0(\omega) . \quad (14)$$

Again, it can be inferred that averaging of complex spectra in the frequency domain can reduce noise.

Now consider the magnitude of the spectrum in Eq. 13, which is

$$|X_k(\omega)| = |X_0(\omega) + N_k(\omega)| . \quad (15)$$

The expectation of the magnitude is

$$\langle |X_k(\omega)| \rangle = \langle |X_0(\omega) + N_k(\omega)| \rangle . \quad (16)$$

It is evident that noise persists in the magnitude although the averaging is carried out with an infinite number of measurements. A similar relation is held true when the averaging scheme is introduced at any further stage of the parameter extraction process. In conclusion, applying a nonlinear operator, e.g., an absolute, to the data before taking an average prohibits noise reduction.

2.3.2 Phase Unwrapping

The phase of a transfer function is a vital part in determining the optical constants. The phase spectrum obtained directly from an angle between the real and imaginary parts of a transfer function essentially wraps around $-\pi$ and π , i.e., whenever the absolute value of the phase is greater than π , it will jump to the opposite polarity by 2π . Phase-jumping causes discontinuity artefacts in a phase spectrum. Figure 3 illustrates the phase wrapping of measured terahertz data. A standard approach to

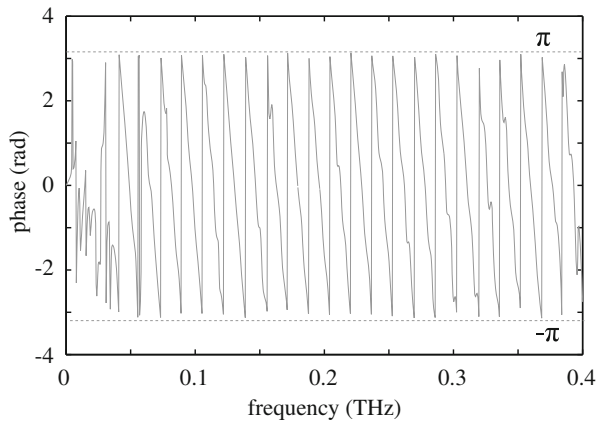


Fig. 3 Phase wrapping. The phase of the transfer function obtained from measurement of a PMMA sample is wrapped around $-\pi$ and π

phase unwrapping can resolve a wrapped phase by adding to or subtracting from the phase spectrum multiples of 2π , or mathematically

$$\phi(\omega) = \angle H(\omega) - 2\pi M(\omega), \quad (17)$$

where M is an integer, counting the number of phase discontinuities in the frequency range lower than ω .

A complication of phase unwrapping arises due to signal noise. For a terahertz spectrum, a reliable part with sufficient signal-to-noise ratio roughly lies between 0.1 and 3 THz. At lower and higher frequencies, the noise plagues the magnitude and phase data, and can introduce artificial phase discontinuities. Unwrapping the phase starting from the noisy part at low frequencies causes error to propagate towards the phase at higher frequencies. An extra step must be taken to avoid false unwrapping. The adapted phase unwrapping scheme discards the noisy phase at low frequencies, and carries out a normal unwrapping only with the reliable phase part. A missing phase profile at low frequencies down to DC is then extrapolated from the unwrapped phase at higher frequencies. In most cases the assumption of a linear phase is sufficient [4]. The whole phase profile is then forced to start from 0 rad at dc. Figure 4 shows a comparison between the results obtained from normal unwrapping and extrapolated unwrapping. The refractive index of PMMA obtained from parameter extraction with no phase extrapolation exhibits large error (the correct index of PMMA is ≈ 1.6).

3 System Characteristics and Limitations

This section discusses various characteristics and limitations associated with THz-TDS systems. It covers the dynamic range, signal-to-noise ratio, frequency

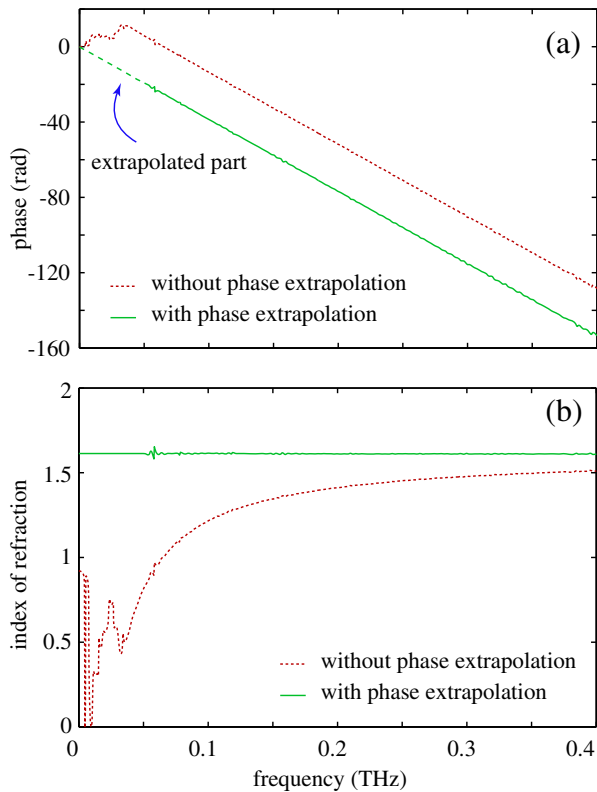


Fig. 4 Phase unwrapping. **a** The phase of the transfer function, obtained from the measurement of a PMMA sample, is unwrapped with and without phase extrapolation. The phase between 0.0 and 0.05 THz is linearly extrapolated from that between 0.05 and 0.1 THz. **b** The index of refraction is determined by using the phases in **a**. The reported value of the refractive index of PMMA at terahertz frequencies is around 1.6 [11]

resolution, and beam properties [12]. All these aspects are critical to the precision and accuracy in THz-TDS measurements. They should always be considered in the course of measurements to avoid false interpretation of results.

3.1 Dynamic Range

Two specific aspects are involved when the dynamic range of THz-TDS is considered [13]. The first is that the data are acquired as time-domain traces, whereas measured optical parameters are derived from the Fourier-transform spectra. The dynamic range of time-domain signals may differ by orders of magnitude from that of the corresponding spectra, and there is no simple analytical relationship between the two. Second, the dynamic range of spectral data is strongly frequency-dependent, and typically decreases steeply with frequency.

The dynamic range is defined as the ratio between the largest and smallest measurable signal, and therefore describes the maximum quantifiable signal change. In practical terms it is calculated as:

$$\text{DR} = \frac{E_{\max}}{N_{\text{rms}}} , \quad (18)$$

where DR denotes the dynamic range, E_{\max} the maximum signal amplitude, and N_{rms} the root-mean-square of the noise floor. It is clear from this expression that the dynamic range of THz-TDS in the frequency domain will follow the spectral profile of its signal amplitude, as seen in Fig. 5. It is a widely accepted practice to quote the maximum value (in this case 2000) as the dynamic range of THz-TDS. Provided that the frequency dependence of the DR is borne in mind, this approach is justifiable to a degree, because the great majority of THz-TDS produce similar spectral profiles. Nevertheless, it would be preferable to quote the DR values at a range of frequencies, or to provide a DR frequency profile.

One important consequence of this frequency dependence of the dynamic range is its effect on the measurement bandwidth. This was first discussed by Jepsen and Fischer [14], where they point out that the maximum absorption coefficient α_{\max} that is measurable in a transmission-mode system is limited by the dynamic range via the relation:

$$\alpha_{\max} l = 2 \ln \left[\text{DR} \frac{4n_s}{(n_s + 1)^2} \right] , \quad (19)$$

where l is the sample thickness and n_s is the sample refractive index. Since the dynamic range of a THz-TDS spectrum decreases with frequency, while the sample absorption typically increases, Eq. 19 sets a limit on the effective measurement bandwidth of optical parameters. Figure 6 demonstrates the concept using measured data. At the point where $\alpha = \alpha_{\max}$, the data becomes very noisy and decreases in line with the α_{\max} curve. In interpreting the absorption (or transmission) data, this is a visual

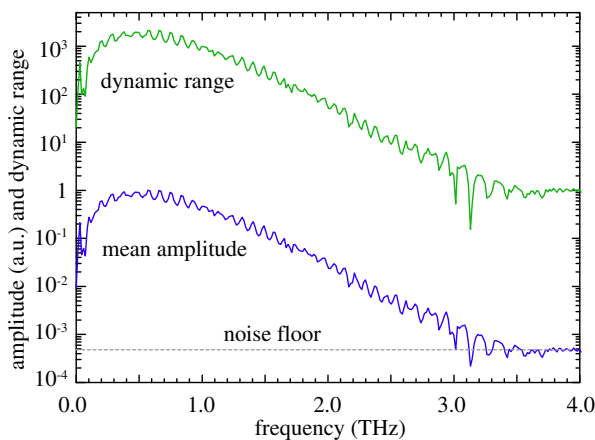


Fig. 5 The terahertz spectrum and the corresponding dynamic range. The spectrum is calculated from a time-domain mean of nine scans. The dynamic range is calculated as the ratio of the amplitude and the noise floor, according to Eq. 18

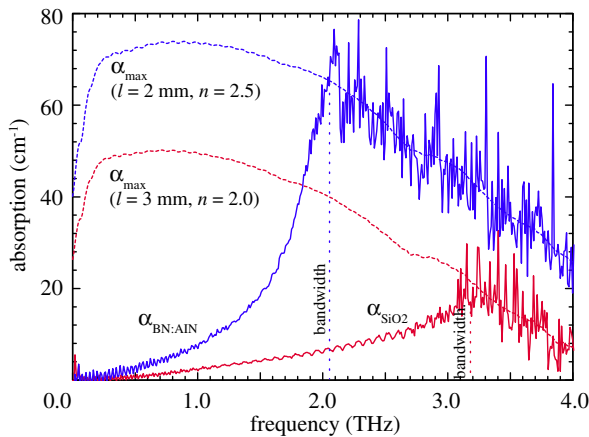


Fig. 6 The relationship between the dynamic range and measurement bandwidth. The maximum measurable absorption, α_{\max} , is calculated for two samples: fused silica (SiO_2 , $l = 3 \text{ mm}$, $n = 2.0$), and ceramic BIN77 (50BN:50AlN, $l = 2 \text{ mm}$, $n = 2.5$); α_{\max} is larger for the thinner sample. It is seen that absorption cannot be measured beyond α_{\max} , and that this limits the measurement bandwidth

indicator that the dynamic range of the system has been exceeded and that the data from that point onwards are no longer meaningful. Note also that it follows from Eq. 19 that the maximum measurable value of absorption is inversely proportional to the sample thickness.

3.2 Signal-to-Noise Ratio

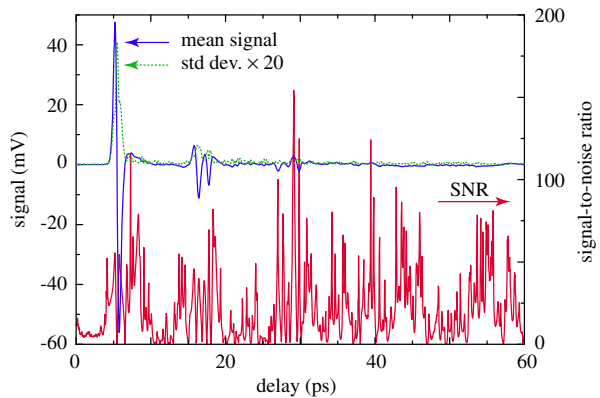
The signal-to-noise ratio (SNR) indicates the minimum detectable signal change, and as such is a complementary system parameter to the dynamic range. Whereas the dynamic range determines the measurement bandwidth, the SNR reflects the amplitude resolution or sensitivity. The SNR is defined as:

$$\text{SNR} = \frac{\overline{E}}{s_E}, \quad (20)$$

where \overline{E} is the mean amplitude and s_E is the corresponding standard deviation. Similarly to the dynamic range, the SNR is different for the temporal and spectral data, and is frequency dependent [13]. Figure 7 shows a typical time-domain trace averaged from nine scans, together with the standard deviation of the data and the SNR. It is seen that the standard deviation is signal-dependent, being largest where the signal is strongest. The SNR is also strongly variable and irregular, and therefore in this case is a poor indicator of the amplitude resolution.

The SNR of the calculated spectrum is shown in Fig. 8. Although it is ‘noisy’, it is far more regular than the time-domain SNR in Fig. 7, and roughly follows the spectral profile of the signal. The empirical observation that the standard deviation (SD) of the terahertz spectral amplitude is proportional to the amplitude itself led Tripathi et al. [15] to derive a simple method for estimating the standard deviation

Fig. 7 Signal-to-noise ratio for time-domain data. The mean and standard deviation are obtained by averaging nine scans. The SNR is calculated as the ratio between the mean value and its standard deviation, according to Eq. 20



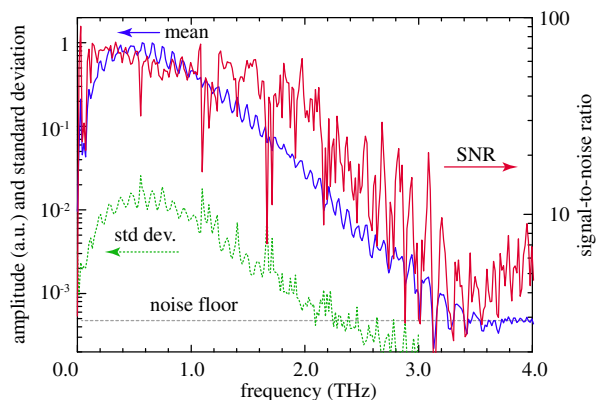
of absorption coefficients. A rigorous treatment of the standard deviation is given in Section 4 in the framework of an uncertainty analysis.

An important consequence of typical values of the dynamic range and SNR for a terahertz system is that a large dynamic range allows examination of strongly attenuating samples, while a low SNR limits the measurement accuracy, particularly for thin samples [16, 17]. Notably, the dynamic range in the time domain is much larger than that in the frequency domain. In some applications this aspect can be utilized for frequency-averaged monitoring or imaging of highly lossy samples.

3.3 Frequency Resolution

The spectral resolution of a terahertz system is determined from the span of the time delay sweep, and is given by $c/2L$, where L is the physical length of the mechanical delay line. In a noise-free system with an unlimited delay line, the resolution would be limited by the pulse repetition rate of the pump laser. However, in the presence of noise the achievable frequency resolution is much poorer, and is determined by the SNR of the system in the time domain. That is because, as the signal amplitude diminishes with an increasing delay from the main pulse, the SNR approaches unity.

Fig. 8 Signal-to-noise ratio for measured spectra. The mean and standard deviation are obtained by averaging nine scans in the frequency domain. The SNR is calculated as the ratio between the mean value and its standard deviation, according to Eq. 20



From that point onwards, scanning to longer delay spans adds no further data: thus the usable delay span is limited by the system SNR. Micken et al. [18] studied the dependence of the frequency resolution on the noise level, and concluded that in a typical system the resolution is in the order of 1 GHz. In experimental practice, it is advisable to limit the scan length to the region where the SNR remains above 2.

Many THz-TDS systems, particularly commercial models, employ fast shakers with a restricted delay range. It is common practice to increase the apparent frequency resolution of the system by zero-padding, i.e., extending the time-domain data set by supplementing it with a string of zeros. Zero padding utilizes the information contained in the data time span by forcing the transform to interpolate additional frequency data points, which trace out the spectral features with greater resolution. The additional data points arising from a string of zeros carry no additional information, but rather interpolate the existing information. Nevertheless, provided that the measured spectrum lacks narrow-frequency features, the method works very well, producing spectra that are negligibly different from high-resolution ones. Due to the time-frequency relationship embodied in the Fourier Transform, narrow spectral features require extended time data in order to be determined accurately. Broader features, however, can be derived accurately from shorter time spans. An example of zero-padding and its effects is shown in Fig. 9 which plots an absorption line of water vapor at 0.557 THz obtained with high resolution, low resolution and zero padding. It is seen that all points in the unpadded spectrum coincide with those of the padded spectrum, whilst the latter also contains additional points that fill out and thus refine the spectral profile. Nevertheless, the padded spectrum does not entirely succeed in reproducing the detailed long-scan spectrum.

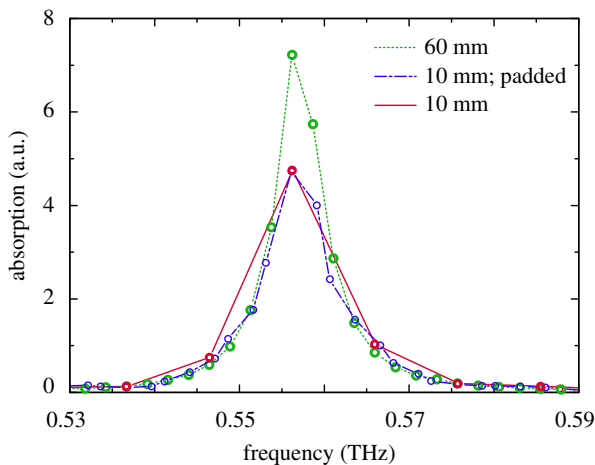


Fig. 9 An absorption line of water vapor at 0.557 THz. The measurements are conducted with a 60-mm scan with 2.5 GHz resolution, a 10-mm scan with zero-padding to 60 mm, also nominally 2.5 GHz resolution, and a 10 mm scan with 15 GHz resolution

3.4 Beam Properties

THz-TDS systems typically employ parabolic mirrors to guide terahertz beams. Most commonly these are 90° off-axis parabolics, which accept a divergent beam from a point source and reflect it to a collimated beam at 90° (or vice versa), as depicted in Fig. 10. Correct alignment of the parabolics is necessary for the following reasons: to maximize the amplitude of the terahertz beam arriving at the detector; to obtain good beam quality; and to ensure correct overlap between the terahertz and the optical probe beams.

Maximizing the terahertz amplitude at the detector increases the signal, and therefore the dynamic range. It may also increase the bandwidth of the detected terahertz signal, because misalignment losses are very often frequency-dependent, with higher frequencies being more sensitive to errors in mirror position and orientation. Likewise, correct terahertz-probe overlap helps to increase the detected signal. Moreover, incorrect overlap may cause non-linearity of the amplitude measurement scale, as discussed in Section 5.2.

An important issue in designing and aligning a THz-TDS system is the acceptance angle for terahertz radiation emitted by the source, i.e., the angle of the radiation cone leaving the emitter and reaching the detector. Lin et al. [19] have analyzed the propagation of terahertz radiation from sub-wavelength sources and have shown that in a typical TDS system the detected terahertz power may be limited by the acceptance angle in a frequency-dependent relationship. As seen in Fig. 11, the power loss is increasingly severe at lower frequencies, causing the observed spectrum to be distorted by disproportionate loss at low frequencies. In practice, the acceptance angle is set by the diameter and focal length of the parabolic mirror collecting radiation from the emitter: therefore it is advisable to use a large-diameter mirror with a short focal length.

For this reason many THz-TDS systems employ hyper-hemispherical lenses mounted on the front of the emitter (and detector), which reduce the divergence of the terahertz beam to approximately 30° [20]. This technique greatly increases the detected terahertz signal, but can result in a number of issues. First, the parabolics are aligned on the assumption that the emitter is a point source, so the emitter-mounted

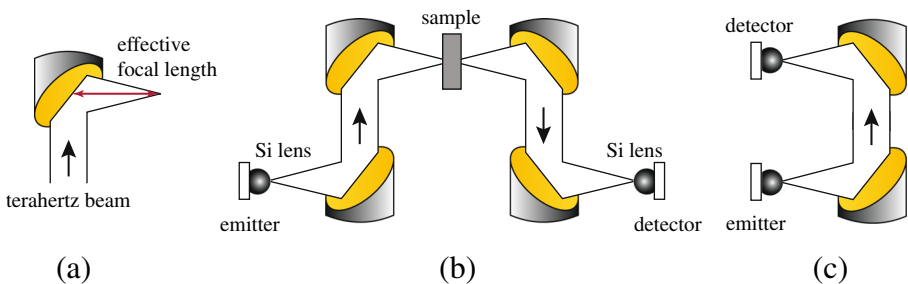


Fig. 10 Terahertz beam guidance with parabolic mirrors. **a** Schematic beam diagram of a 90° off-axis parabolic mirror. **b**, **c** Two commonly used mirror configurations in THz-TDS: 4-mirror and 2-mirror, respectively

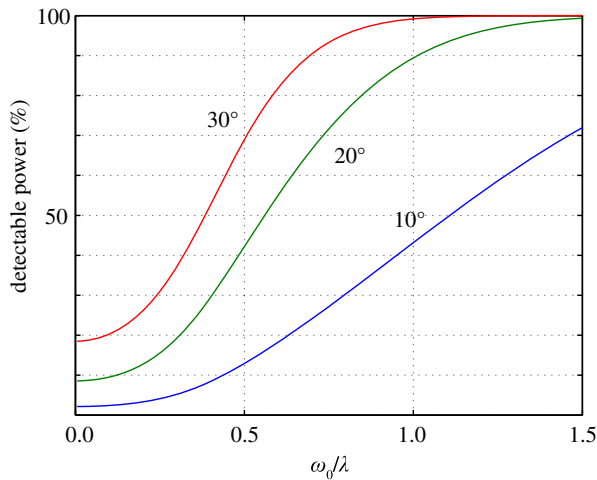


Fig. 11 Detectable fraction of terahertz power for three different acceptance angles. The horizontal axis is the normalized infrared pump beam waist, w_0/λ . Reproduced from [19]

lens severely affects the beam waist and wavefront all along its path through the system. Moreover, a high degree of accuracy is required in aligning the axis of the lens to be centered on the terahertz source and collinear with the emitted terahertz radiation: for a 2 mm diameter lens the required accuracy is $<150\ \mu\text{m}$ [21].

The effects of emitter-mounted lenses on the terahertz beam propagation have been intensively modelled and studied experimentally [20–27]. It has been shown that the terahertz beam transmitted by a hyperhemispherical lens is liable to suffer from several adverse consequences, some of which may affect spectral measurements due to frequency dependence, and because they may be further exacerbated by placing optically thick samples in the beam path:

- the beam does not behave like a TEM_{00} Gaussian [22]
- the beam exhibits complex frequency-dependent spatial profiles, often asymmetric, with strong diffraction lobes [20–27]
- the bandwidth is limited by the diffraction geometry [20]
- there is a reduction in the emitted power [23]
- the diffraction limit can only be achieved at the lowest frequencies [25]

Materials or objects to be examined by THz-TDS are commonly positioned in the focal plane of the terahertz beam. In part this is done because collimated beams in TDS systems often have large diameters ($<25\ \text{mm}$), while samples are often much smaller or require to be imaged with high spatial resolution. However, the presence of a dielectric object at the beam waist can alter the beam wavefront and beam path, thus affecting measurement, in particular causing significant errors in the refractive index. The effect is related to the Gouy shift, and has been examined specifically in relation to errors in TDS measurements by Bowen et al. [26] and Choi et al. [27]. An example of refractive index error observed when using a focused as opposed to a

collimated beam is demonstrated in Fig. 12; such errors become more significant in samples with a large optical thickness.

4 Measurement Uncertainties: Sources and Evaluation

This section discusses various sources of error existing in transmission-mode THz-TDS measurements, inherent from the system and parameter estimation process. An analysis on the signal amplitude error is given to quantify its impact on the estimated optical constants. This uncertainty evaluation allows to compare impacts from different sources of error, and offers a standard for comparison of results among different measurements. Further to that, the evaluation provides a basis for optimization of measurement parameters to improve the measurement precision and accuracy.

4.1 Sources of Error in THz-TDS Measurement

Many sources of randomness affecting a THz-TDS signal have been reported so far. These sources include laser intensity fluctuation [28–30], optical and electronic noise [31, 32], delay line jitter [33], registration error [34], and so on. Mathematical treatment for these noise sources is available in general. Contributions to the error in the estimated optical constants are not only from the randomness in the signal, but also from imperfections in the physical setup and parameter extraction process. These imperfections relate to, for example, the sample thickness measurement, the sample alignment, and so on.

Significant sources of error are shown in Fig. 13, where they are listed along with the parameter extraction process and accompanied by their class (random or systematic). In addition to noise, the sample signal also contains reflections, which, if not dealt with appropriately, cause a systematic error. The error in the amplitude

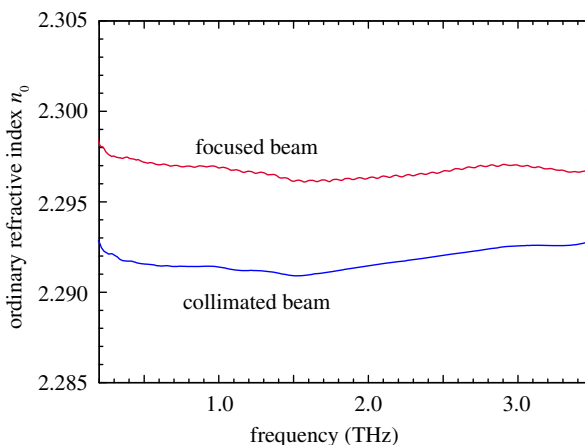


Fig. 12 Influence of the terahertz beam on an extracted material parameter. A 5 mm thick pyrolytic boron nitride is measured for its refractive index using a collimated and a focused terahertz beam

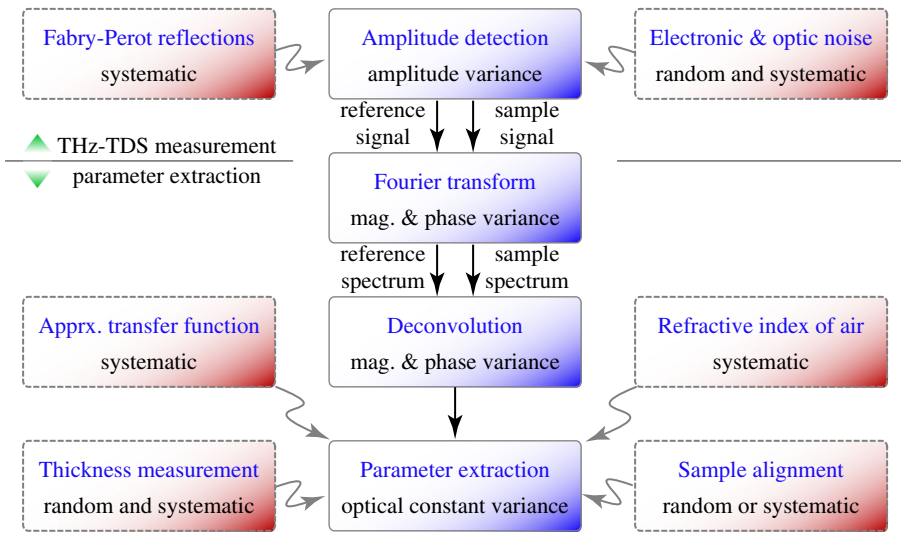


Fig. 13 Sources of error in THz-TDS measurement. The sources of error in the red dashed boxes occur in both the THz-TDS measurement and the parameter extraction process. The errors produced by these sources are classified as either random or systematic. They cause the variances and deviations, which propagate down the process, and eventually contribute to the uncertainty in the extracted optical constants

from several measurements manifests itself as a variance (or deviation). It propagates down the parameter extraction process, through to the Fourier transform and deconvolution stages, producing the variance in the magnitude and phase of the estimated transfer function. The parameter extraction process requires knowledge of the sample thickness, sample alignment, and air refractive index, each of which have a degree of uncertainty. This step introduces the variances to the estimation. Furthermore, an approximation to the model transfer function gives rise to a systematic error. At the output, all these variances accumulate and contribute to the uncertainty in the extracted optical constants. It should be noted that the amplitude variance is a dominant contributor to the measurement uncertainty. The next subsection will demonstrate an analytical expression that quantifies the impact of the amplitude variance on the estimated optical constants. Extensive analyses on other sources of error can be found elsewhere [35].

4.2 Evaluation of Error in Signal Amplitude

The terahertz amplitude is prone to variation induced by many sources of random and systematic errors. As mentioned earlier, the sources of random error include laser intensity fluctuation, optical and electronic noise, jitter in the delay stage, etc., whereas the sources of systematic error include registration error, mechanical drift, etc. The variation in the amplitude may embrace the effects from inhomogeneity in a sample or among samples, if the sample is displaced or replaced with nominally identical samples during several measurements. What is considered here is the amplitude

variance model, which combines all these errors and assumes a normal probability distribution. This treatment is valid although systematic error is involved, since the systematic error drifts over time and thus cannot be tackled by the method that requires a constant systematic error [36].

Given the amplitude variances of the time domain reference and sample signals, denoted by $s_{E_{\text{ref}}}^2(k)$ and $s_{E_{\text{sam}}}^2(k)$, respectively, the amplitude-related variances in the optical constants read

$$s_{n,E}^2(\omega) = \left(\frac{c}{\omega l}\right)^2 \left\{ \frac{A_{\text{sam}}(\omega)}{|E_{\text{sam}}(\omega)|^4} + \frac{A_{\text{ref}}(\omega)}{|E_{\text{ref}}(\omega)|^4} \right\}, \quad (21a)$$

$$s_{\kappa,E}^2(\omega) = \left(\frac{c}{\omega l}\right)^2 \left\{ \frac{B_{\text{sam}}(\omega)}{|E_{\text{sam}}(\omega)|^4} + \frac{B_{\text{ref}}(\omega)}{|E_{\text{ref}}(\omega)|^4} + \left(\frac{n(\omega) - n_0}{n(\omega) + n_0}\right)^2 \frac{s_{n,E}^2(\omega)}{n^2(\omega)} \right\}, \quad (21b)$$

where

$$A_{\text{sam}}(\omega) = \sum_k \Im^2[E_{\text{sam}}(\omega) \exp(j\omega k\tau)] s_{E_{\text{sam}}}^2(k), \quad (22a)$$

$$A_{\text{ref}}(\omega) = \sum_k \Im^2[E_{\text{ref}}(\omega) \exp(j\omega k\tau)] s_{E_{\text{ref}}}^2(k), \quad (22b)$$

$$B_{\text{sam}}(\omega) = \sum_k \Re^2[E_{\text{sam}}(\omega) \exp(j\omega k\tau)] s_{E_{\text{sam}}}^2(k), \quad (22c)$$

$$B_{\text{ref}}(\omega) = \sum_k \Re^2[E_{\text{ref}}(\omega) \exp(j\omega k\tau)] s_{E_{\text{ref}}}^2(k). \quad (22d)$$

Here, k is the temporal index and τ is the sampling interval, and thus $k\tau$ is the time. The summation is carried out over the time duration of a recorded terahertz signal. In the equations, all the parameters are calculated at their mean value.

In Eq. 21a, b, the square of the thickness, l^2 , is a major factor. Increasing the thickness will seemingly decrease the variance in the optical constants. A physical reason behind this is that, for a very thin sample, the system might not be sensitive enough to detect a small change in the amplitude and phase, which is masked by noise. A thicker sample allows terahertz waves to interact more with the material, causing a larger change in signal. But, this competes with the fact that $|E_{\text{sam}}(\omega)| \propto \exp(-l)$ and thus increasing l will lower the amplitude of a sample signal and lift the overall variance. An analytical treatment on the thickness-amplitude tradeoff results in the optimal thickness condition that suggests $l = 2/\alpha(\omega)$, where $\alpha(\omega)$ is the sample absorption coefficient [37].

5 Measurement Calibrations

Terahertz time-domain spectrometers are similar to other types of spectrometer in that they are predominantly employed to measure frequency-dependent optical constants of a wide variety of materials and substances. Clearly, identification and characterisation of spectral features, such as absorption lines, depends on correct calibration of the frequency (or wavelength) scale. For this purpose, UV-visible, near-IR and mid-IR spectrometers use standard absorbing materials with well-known

resonance spectra. However, in the terahertz band few solid materials have narrow resonance absorption lines, and those lines are too few (typically one or two) to provide calibration across the whole band. Therefore other types of frequency calibration artefacts must be sought for THz-TDS.

Because THz-TDS data is acquired in the time domain and then translated into frequency domain via Fourier Transform, the phase information is derived from the delay data of the time-domain scan. As a consequence, calibrating the frequency scale also ensures the correctness of the phase data and the parameters derived from it, e.g. the refractive index. Similarly, in order to have confidence in the measured spectral profile, the amplitude scale of a spectrometer must be linear (or at least have a known function that can be applied as a correction factor). Spectrometers in the visible and infrared only rarely have the linearity of their power response tested or calibrated, since they employ detectors that are tested for linear response at the manufacturing stage and that function independently of the illumination source. Unlike those, THz-TDS operate in a pump-probe configuration, whereby the source and detector form an integral system. The linearity of amplitude response of a THz-TDS depends on multiple factors of signal-probe interaction, including individual alignment of terahertz and probe beams, beam overlap, spatial beam profiles, and temporal pulse shapes. Therefore testing the linearity of a THz-TDS is an essential characterisation step ensuring confidence in its performance.

5.1 Frequency Calibration

The frequency scale of spectrometers in the visible and infrared is commonly calibrated by using standard material artifacts possessing multiple narrow absorption lines whose frequencies are well known and reliably reproduced. In the terahertz band, however, few solid or liquid materials have characteristic resonances, and those generally appear as broad bands; none have multiple narrow absorption peaks such as required of a frequency calibration standard. On the other hand, many gases have their rotational transitions at terahertz frequencies, with narrow linewidths, and are thereby suitable candidates for calibration artifacts.

Perhaps the best known and widely used gas for frequency verification in the terahertz band is atmospheric water vapor that possesses many strong narrow lines. However, although the frequencies of these lines are well known [38, 39], their relative amplitudes vary with environmental conditions [40] such as atmospheric pressure and humidity. Moreover, many of the lines are doublets and triplets, and therefore require very high (sub-GHz) frequency resolution to define their peak maxima and profiles. The spacing of lines is particularly dense at higher frequencies above 2 THz, where the reduced signal-to-noise ratio and dynamic range of THz-TDS systems make accurate measurements far more difficult. Moreover, a calibration standard must by definition be a stable, controllable, well-defined artifact. Ambient humidity clearly cannot serve in such role. A sealed air cell with defined humidity is a possible solution, but over time and if subject to temperature fluctuations, water adsorption on the cell surfaces may alter its moisture content.

Linear gas molecules have pure rotational spectra consisting of a frequency comb of nearly-equally spaced lines with a distinctive amplitude envelope, where the frequencies, amplitudes and widths of the lines are well understood and intensively documented [41]. The center frequency of the pure rotational line J is given in the first approximation by [42]

$$f_0 = 2B(J + 1) , \quad (23)$$

and its peak absorption coefficient α_0 , defining the band envelope, has the form [42]

$$\alpha_0 = CB^3(J + 1)^3 \exp[-(h/kT)BJ(J + 1)] , \quad (24)$$

where h is the Plank constant, k is the Boltzmann constant, and T is the temperature in Kelvin. The constants B and C are molecule-specific, so that a suitable gas can be chosen to serve the calibration needs. To make a calibration artifact, the chosen gas is encapsulated in a sealed cell with terahertz-transparent windows; examples of such cells are depicted in Fig. 14.

Figure 15 shows the absorption spectra of two gases that may be suitable for calibrating terahertz time-domain spectrometers: CO, with a line spacing of 114 GHz centered at 1.5 THz; and N₂O, with a line spacing of 25 GHz centered at 0.73 THz. Having measured the gas absorption spectrum in the standard cell, the frequency scale of the terahertz spectrometer may be checked by plotting the differences between the measured and expected peak positions, as shown in Fig. 16.

Although gas cells provide a reliable frequency calibration standard, they may be unwieldy to use in some circumstances; they also require careful handling, since the majority of useful gases are highly toxic. Moreover, it may be desirable that a frequency calibration standard should produce regularly spaced peaks across the entire terahertz band, of a uniform size and with a well-defined profile. This can be achieved by employing an etalon, which also has the advantage of being inexpensive, small, and convenient to use. The method utilizes the echoes produced by multiple reflections in thin plane-parallel samples inserted in the terahertz beam [45].

Such an etalon may consist of a silicon wafer of a common type used in semiconductor industry, which for this purpose must be high resistivity and optically polished. High resistivity silicon has negligible absorption in the terahertz band, and due to its high refractive index of 3.42, polished faces provide sufficient reflectivity to perform

Fig. 14 Gas cells with PTFE windows used at NPL as terahertz frequency calibration artifacts. PTFE has no absorption features below 5 THz



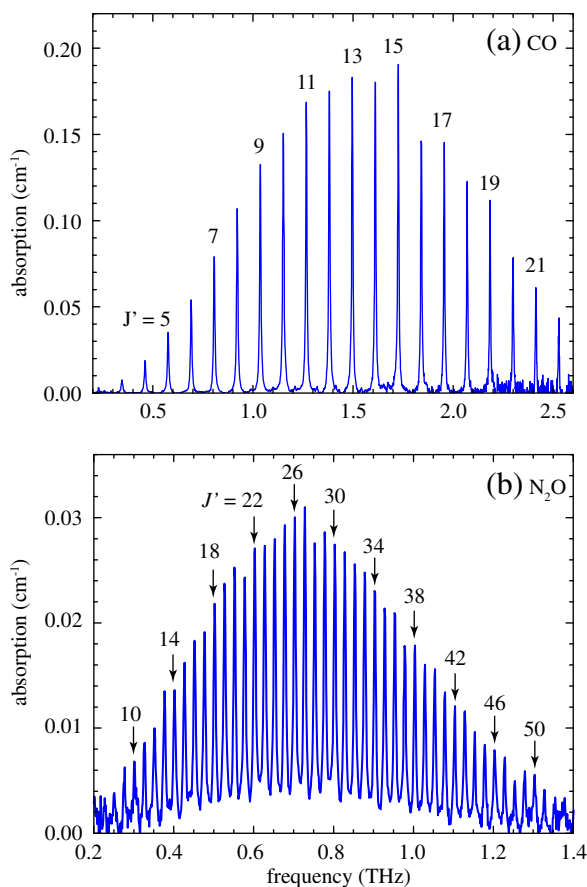


Fig. 15 Absorption spectra of different gases. **a** CO at 2.0 bar ($2B = 114$ GHz) [43], and **b** N₂O at 1.2 bar ($2B = 25$ GHz) [44]

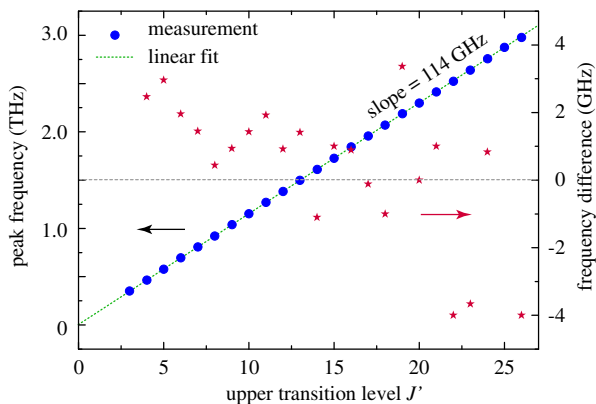


Fig. 16 Comparison of the absorption lines obtained from the measurement and database. *Left*: Measured frequencies of CO absorption lines. *Right*: Deviation from the HITRAN database [41]

as an etalon. Figure 17 depicts the measured transmission spectrum of a silicon wafer etalon together with the model.

The peaks and troughs in the etalon spectrum occur at frequencies given by, respectively, [46]

$$f_N = \frac{c}{2nl}N, \quad \text{and} \quad f_{N+1/2} = \frac{c}{2nl}(N + 1/2), \quad (25)$$

where n is the refractive index of the etalon material and l is its thickness. The integer N is the order of the peak. The peak/trough frequencies carry uncertainty arising from the uncertainty in the etalon thickness measurement, such that $\Delta f/f = -\Delta l/l$. The thickness of the etalon may be chosen so as to provide the desirable frequency spacing.

The amplitude transmission of an etalon as a function of frequency f , shown in Fig. 17, can be calculated from [46]

$$T = \left[1 + \frac{4R}{(1-R)^2} \sin^2 \left(\frac{n\omega d}{c} \right) \right]^{-\frac{1}{2}}, \quad (26)$$

where

$$R = \left(\frac{n-1}{n+1} \right)^2. \quad (27)$$

The peak/trough frequencies provide frequency calibration, while the transmission spectrum can be used to verify the measurement of the spectral amplitude profile.

The simplest method of checking the frequency scale of a terahertz system is to record the frequencies of the peaks and troughs in the transmission spectrum of the etalon and to compare them with those calculated from Eq. 26. Similarly to Fig. 16, the difference between the measured and expected frequencies for each peak/trough can then be plotted as a function of its position, as shown in Fig. 18. Such a plot

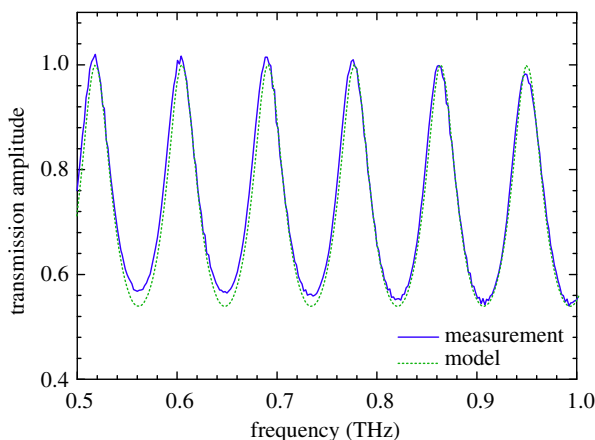


Fig. 17 Partial terahertz transmission spectrum with an etalon effect. The measurement is carried out with a 438 μm thick silicon wafer etalon, measured and calculated from Eq. 26

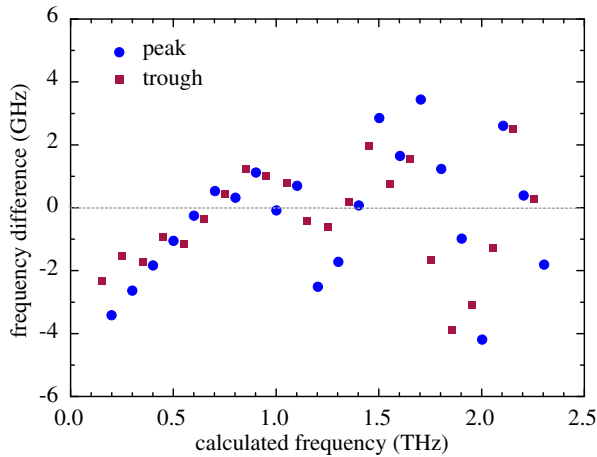


Fig. 18 Differences between the measured and expected peak/trough frequencies. As in Fig. 17, the measurement is conducted by using a 438 μm thick silicon wafer etalon with a free spectral range of 100 GHz. The expected peak/trough frequencies are obtained from Eq. 26

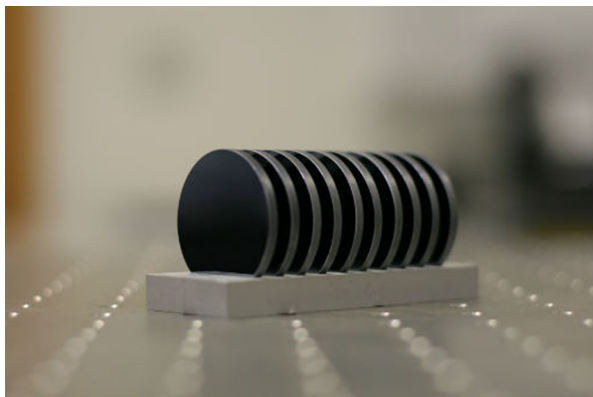
reveals any systematic frequency errors, as well as the digitizing errors and the noise in the data. It also helps to identify the band over which frequency measurements are valid within a defined uncertainty.

5.2 Amplitude Linearity Calibration

The analysis and interpretation of terahertz data assume that the amplitude response of a THz-TDS system is linear, i.e., that the recorded signal is linearly proportional to the terahertz field across the entire dynamic range of the system. The assumption of linearity forms the basis of spectral measurements and the optical constants derived from them. However, in practice, the linearity of THz-TDS data acquisition is seldom tested.

Testing amplitude linearity of a THz-TDS system requires a calibration artifact having two main attributes: (i) an attenuation that is well defined and constant across the usable bandwidth, and (ii) accurate and equal attenuation steps spanning the dynamic range of the system. The solution developed at NPL employs as “loss elements” a stack of optically flat high-resistivity silicon plates [47]. As already mentioned, high-resistivity silicon has negligible absorption and dispersion in the terahertz band, and therefore transmission loss through a silicon plate is due solely to Fresnel reflection. The loss produced by a stack of plates separated by air gaps is multiplicative, to the power equal to the number of plates in the stack. In the NPL test kit, depicted in Fig. 19, each silicon plate is 3 mm thick with 3 mm air gaps between plates: the plates are robust and easy to handle; the thickness is sufficient to allow time-gating of reflections in test scans; and the total length of the device is conveniently short.

Fig. 19 The amplitude linearity calibration artifact used by NPL. It consists of 10 high-resistivity Si plates, each of 3 mm thick separated with 3 mm air gaps



In the absence of absorption and Fabry-Pérot effect, from Eq. 7 the amplitude component of the transfer function affected by reflection loss for a stack of N plates is equal to

$$|H_N| = \left(\frac{4n_s}{[n_s + 1]^2} \right)^N. \quad (28)$$

For silicon, $n_s = 3.42$ and therefore the transmission factor per each silicon plate is $|H_1| = 0.7$.

The simplest method of linearity calibration is to test the linearity of the time-domain signal by plotting the amplitude of the time-domain peak against the number of silicon plates in the beam path. For a linear system, a semi-log plot of the data will be linear with a slope of 0.7, as in Fig. 20. This provides a frequency-averaged test of the system response, with no spectral information. It is seen that at low signal levels where the system approaches its noise floor there is a slight deviation from linearity.

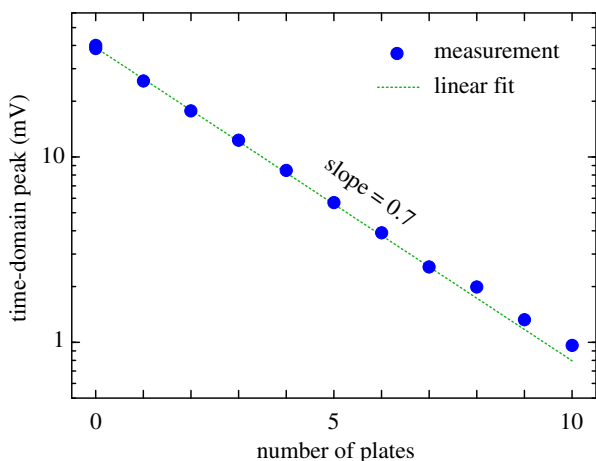


Fig. 20 Amplitude linearity test of the time-domain peak (frequency-averaged)

The deviation is positive because the peak amplitude must always be positive, and therefore the average of the noise has a positive value, so that the error increases with the relative noise.

A more detailed, frequency-resolved method of testing the linearity of a terahertz system involves calculating the spectral amplitudes at chosen frequencies. Those amplitude values are then plotted against the number of silicon plates in the beam path, as seen in Fig. 21a. As previously, the semi-log plots are expected to be linear with a slope of 0.7. Increased positive errors at higher frequencies indicate the limits of the system dynamic range. The data at 3 THz show the strongest deviation, because at that frequency the system is close to its noise floor, with the dynamic range below 10.

The linearity of a terahertz system should not be assumed, but ought to be experimentally verified. An example of a system that is severely nonlinear due to misalignment is shown in Fig. 21b, where the system is seen to deviate most strongly

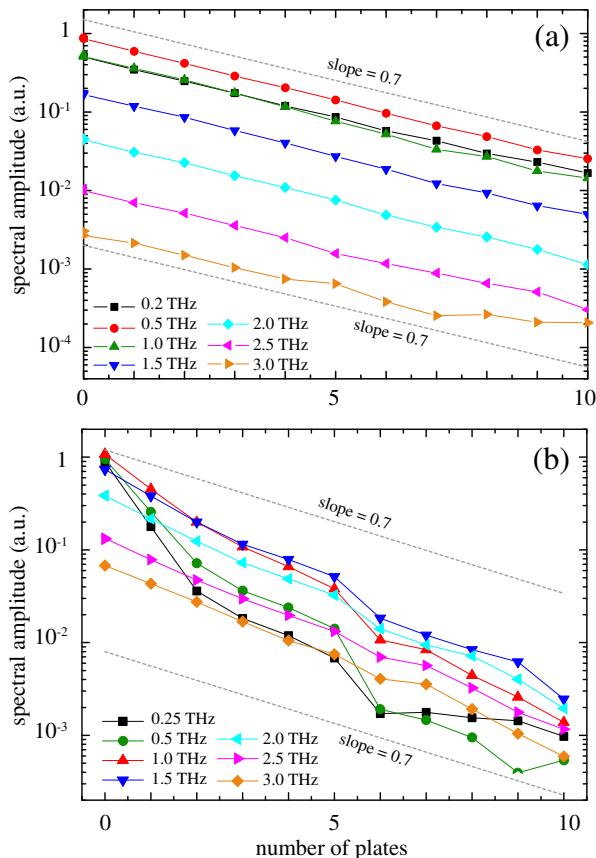


Fig. 21 Frequency-resolved linearity tests on a THz TDS. **a** After system re-alignment, showing satisfactory linearity, and **b** before system re-alignment, showing severe non-linearity

at low frequencies. The nonlinearity may be caused by an imperfection in the terahertz/optical beam overlap inside the detector crystal (ZnTe): the effect is strongest at low frequencies where the diffraction-limited waist of the terahertz beam is largest. This may have been exacerbated by the imperfect collimation of the terahertz beam: placing Si plates in the beam would cause the beam waist to shift position and would further affect the terahertz-probe overlap. Figure 21a shows results from the same system after thorough re-alignment, when the terahertz and optical beams are accurately overlapped. This resulted in nonlinearities being drastically reduced, demonstrating that simple measures, such as attention to correct alignment, can significantly improve linearity of the amplitude response of a THz-TDS system.

A somewhat similar approach using multiple internal reflections in a single silicon wafer was demonstrated by Withayachumnankul et al. [48]. Although this method has the advantage of a simpler and smaller calibration artifact, it also has the disadvantages of only a few available attenuation steps obtainable from reflections (typically 3) and the difficulty of performing spectral analysis on the reflection peaks.

6 Conclusion

We have discussed the importance of metrological aspects of THz-TDS measurements and presented an overview of particular issues and solutions. The calculations involved in signal processing and parameter extraction were reviewed and the errors arising from them highlighted. In particular, the importance of correct phase unwrapping was demonstrated. System performance was discussed, together with limitations on resolution, bandwidth, and accuracy arising from inherent aspects of system operation. It was shown that the measurement bandwidth is limited by the dynamic range, whilst the achievable frequency resolution is determined by the SNR. Uncertainty analysis and sources of error were detailed. Finally, calibration procedures for frequency and amplitude linearity were described.

References

1. D. H. Auston, K. P. Cheung, and P. R. Smith, "Picosecond photoconducting Hertzian dipoles," *Applied Physics Letters*, vol. 45, no. 3, pp. 284–286, 1984.
2. M. V. Klein, *Optics*. New York: John Wiley & Sons, 1970.
3. D. Grischkowsky, S. Keiding, M. van Exter, and C. Fattinger, "Far-infrared time-domain spectroscopy with terahertz beams of dielectrics and semiconductors," *Journal of the Optical Society of America B: Optical Physics*, vol. 7, no. 10, pp. 2006–2015, 1990.
4. L. Duvillaret, F. Garet, and J.-L. Coutaz, "A reliable method for extraction of material parameters in terahertz time-domain spectroscopy," *IEEE Journal of Selected Topics in Quantum Electronics*, vol. 2, no. 3, pp. 739–746, 1996.
5. L. Duvillaret, F. Garet, and J.-L. Coutaz, "Highly precise determination of optical constants and sample thickness in terahertz time-domain spectroscopy," *Applied Optics*, vol. 38, no. 2, pp. 409–415, 1999.
6. T. Dorney, R. Baraniuk, and D. Mittleman, "Material parameter estimation with terahertz time-domain spectroscopy," *Journal of the Optical Society of America A: Optics, Image Science, and Vision*, vol. 18, no. 7, pp. 1562–1571, 2001.

7. I. Pupeza, R. Wilk, and M. Koch, “Highly accurate optical material parameter determination with THz time-domain spectroscopy,” *Optics Express*, vol. 15, no. 7, pp. 4335–4350, 2007.
8. M. Scheller and M. Koch, “Fast and accurate thickness determination of unknown materials using terahertz time domain spectroscopy,” *Journal of Infrared, Millimeter, and Terahertz Waves*, vol. 30, no. 7, pp. 762–769, 2009.
9. M. Scheller, C. Jansen, and M. Koch, “Analyzing sub-100- μm samples with transmission terahertz time domain spectroscopy,” *Optics Communications*, vol. 282, no. 7, pp. 1304–1306, 2009.
10. B. M. Fischer, M. Hoffmann, and P. U. Jepsen, “Dynamic range and numerical error propagation in terahertz time-domain spectroscopy,” in *Optical Terahertz Science and Technology, Technical Digest (CD)*, Optical Society of America, 2005. paper TuD1.
11. Y.-S. Jin, G.-J. Kim, and S.-G. Jeon, “Terahertz dielectric properties of polymers,” *Journal of the Korean Physical Society*, vol. 49, no. 2, pp. 513–517, 2006.
12. M. Naftaly, “Metrology issues and solutions in THz time domain spectroscopy: noise, errors, calibration,” *IEEE Sensors Journal*, vol. 13, no. 1, pp. 8–17, 2013.
13. M. Naftaly and R. Dudley, “Methodologies for determining the dynamic ranges and signal-to-noise ratios of terahertz time-domain spectrometers,” *Optics Letters*, vol. 34, no. 8, pp. 1213–1215, 2009.
14. P. U. Jepsen and B. M. Fischer, “Dynamic range in terahertz time-domain transmission and reflection spectroscopy,” *Optics Letters*, vol. 30, no. 1, pp. 29–31, 2005.
15. S. R. Tripathi, M. Aoki, K. Mochizuki, I. Hosako, T. Asahi, and N. Hiromoto, “Practical method to estimate the standard deviation in absorption coefficients measured with THz time-domain spectroscopy,” *Optics Communications*, vol. 283, no. 12, pp. 2488–2491, 2010.
16. J. F. O’Hara, W. Withayachumnankul, and I. Al-Naib, “A review on thin-film sensing with terahertz waves,” *Journal of Infrared, Millimeter, and Terahertz Waves*, vol. 33, no. 3, pp. 245–291, 2012.
17. W. Withayachumnankul, “Limitation in thin-film detection with transmission-mode terahertz time-domain spectroscopy,” *arXiv preprint arXiv:1111.3498*, 2011.
18. S. P. Mickan, J. Xu, J. Munch, X.-C. Zhang, and D. Abbott, “The limit of spectral resolution in thz time-domain spectroscopy,” in *SPIE Microelectronics, MEMS, and Nanotechnology*, pp. 54–64, International Society for Optics and Photonics, 2004.
19. H. Lin, C. Fumeaux, B. M. Fischer, and D. Abbott, “Modelling of sub-wavelength THz sources as gaussian apertures,” *Optics Express*, vol. 18, no. 17, pp. 17672–17683, 2010.
20. J. Van Rudd and D. M. Mittleman, “Influence of substrate-lens design in terahertz time-domain spectroscopy,” *Journal of the Optical Society of America B: Optical Physics*, vol. 19, no. 2, pp. 319–329, 2002.
21. D. F. Filipovic, G. P. Gauthier, S. Raman, and G. M. Rebeiz, “Off-axis properties of silicon and quartz dielectric lens antennas,” *IEEE Transactions on Antennas and Propagation*, vol. 45, no. 5, pp. 760–766, 1997.
22. M. T. Reiten, S. A. Harmon, and R. A. Cheville, “Terahertz beam propagation measured through three-dimensional amplitude profile determination,” *Journal of the Optical Society of America B: Optical Physics*, vol. 20, no. 10, pp. 2215–2225, 2003.
23. P. U. Jepsen and S. Keiding, “Radiation patterns from lens-coupled terahertz antennas,” *Optics Letters*, vol. 20, no. 8, pp. 807–809, 1995.
24. R. Rungsawang, K. Ohta, K. Tukamoto, and T. Hattori, “Ring formation of focused half-cycle terahertz pulses,” *Journal of Physics D: Applied Physics*, vol. 36, no. 3, pp. 229–235, 2003.
25. A. Bitzer, H. Helm, and M. Walther, “Beam-profiling and wavefront-sensing of thz pulses at the focus of a substrate-lens,” *IEEE Journal of Selected Topics in Quantum Electronics*, vol. 14, no. 2, pp. 476–481, 2008.
26. J. Bowen, G. Walker, S. Hadjiloucas, and E. Berry, “The consequences of diffractively spreading beams in ultrafast THz spectroscopy,” in *Conference Digest of the 2004 Joint 29th International Conference on Infrared and Millimeter Waves, 2004 and 12th International Conference on Terahertz Electronics, 2004*, pp. 551–552, IEEE, 2004.
27. D. Choi, H. Son, H. Park, and G. Park, “Focused beam effect on measuring precise optical parameters of liquid water with terahertz time domain spectroscopy,” in *36th International Conference on Infrared, Millimeter and Terahertz Waves (IRMMW-THz), 2011*, pp. 1–2, IEEE, 2011.
28. J. Son, J. V. Rudd, and J. F. Whitaker, “Noise characterization of a self-mode-locked Ti:sapphire laser,” *Optics Letters*, vol. 17, no. 10, pp. 733–735, 1992.
29. H. A. Haus and A. Mecozzi, “Noise of mode-locked lasers,” *IEEE Journal of Quantum Electronics*, vol. 29, no. 3, pp. 983–996, 1993.

30. A. Poppe, L. Xu, F. Krausz, and C. Spielmann, “Noise characterization of sub-10-fs Ti:sapphire oscillators,” *IEEE Journal of Selected Topics in Quantum Electronics*, vol. 4, no. 2, pp. 179–184, 1998.
31. M. van Exter and D. R. Grischkowsky, “Characterization of an optoelectronic terahertz beam system,” *IEEE Transactions on Microwave Theory and Techniques*, vol. 38, no. 11, pp. 1684–1691, 1990.
32. L. Duvillaret, F. Garet, and J.-L. Coutaz, “Influence of noise on the characterization of materials by terahertz time-domain spectroscopy,” *Journal of the Optical Society of America B: Optical Physics*, vol. 17, no. 3, pp. 452–460, 2000.
33. J. Letosa, M. García-Gracia, J. M. Forniés-Marquina, and J. M. Artacho, “Performance limits in TDR technique by Monte Carlo simulation,” *IEEE Transactions on Magnetics*, vol. 32, no. 3, pp. 958–961, 1996.
34. N. Cohen, J. W. Handley, R. D. Boyle, S. L. Braunstein, and E. Berry, “Experimental signature of registration noise in pulsed terahertz systems,” *Fluctuation and Noise Letters*, vol. 6, no. 1, pp. L77–L84, 2006.
35. W. Withayachumnankul, B. M. Fischer, H. Lin, and D. Abbott, “Uncertainty in terahertz time-domain spectroscopy measurements,” *Journal of the Optical Society of America B: Optical Physics*, vol. 25, no. 6, pp. 1059–1072, 2008.
36. M. Grabe, “Estimation of measurement uncertainties—an alternative to the ISO guide,” *Metrologia*, vol. 38, pp. 97–106, 2001.
37. W. Withayachumnankul, B. M. Fischer, and D. Abbott, “Material thickness optimization for transmission-mode terahertz time-domain spectroscopy,” *Optics Express*, vol. 16, no. 10, pp. 7382–7396, 2008.
38. R. E. Allman and R. J. Foltynowicz, “Terahertz time-domain spectroscopy of atmospheric water vapor from 0.4 to 2.7 THz,” tech. rep., Sandia National Laboratories, 2005.
39. D. M. Mittleman, R. Jacobsen, R. Neelamani, R. G. Baraniuk, and M. C. Nuss, “Gas sensing using terahertz time-domain spectroscopy,” *Applied Physics B: Lasers and Optics*, vol. 67, no. 3, pp. 379–390, 1998.
40. X. Xin, H. Altan, A. Saint, D. Matten, and R. Alfano, “Terahertz absorption spectrum of para and ortho water vapors at different humidities at room temperature,” *Journal of Applied Physics*, vol. 100, no. 9, pp. 094905–094905, 2006.
41. L. Rothman, I. Gordon, Y. Babikov, A. Barbe, D. C. Benner, P. Bernath, M. Birk, L. Bizzocchi, V. Boudon, L. Brown, *et al.*, “The HITRAN2012 molecular spectroscopic database,” *Journal of Quantitative Spectroscopy and Radiative Transfer*, 2013.
42. G. W. Chantry, *Submillimetre spectroscopy*, vol. 1. Academic Press, London, UK, 1971.
43. W. Aenchbacher, M. Naftaly, and R. Dudley, “Line strengths and self-broadening of pure rotational lines of carbon monoxide measured by terahertz time-domain spectroscopy,” *Applied Optics*, vol. 49, no. 13, pp. 2490–2496, 2010.
44. W. Aenchbacher, M. Naftaly, and R. Dudley, “Line strengths and self-broadening of pure rotational lines of nitrous oxide measured by terahertz time-domain spectroscopy,” *Journal of the Optical Society of America B: Optical Physics*, vol. 27, no. 9, pp. 1717–1721, 2010.
45. M. Naftaly, R. Dudley, and J. Fletcher, “An etalon-based method for frequency calibration of terahertz time-domain spectrometers (THz TDS),” *Optics Communications*, vol. 283, no. 9, pp. 1849–1853, 2010.
46. R. D. Guenther, *Modern optics*. Wiley-VCH, 1990.
47. M. Naftaly and R. Dudley, “Linearity calibration of amplitude and power measurements in terahertz systems and detectors,” *Optics Letters*, vol. 34, no. 5, pp. 674–676, 2009.
48. W. Withayachumnankul, B.-Y. Ung, B. M. Fischer, and D. Abbott, “Measurement of linearity in thz-tds,” in *34th International Conference on Infrared, Millimeter, and Terahertz Waves (IRMMW-THz)*, 2009, pp. 1–2, IEEE, 2009.